PHOTONICS Research

Chirp control of femtosecond-pulse scattering from drag-reducing surface-relief gratings

Juliane Eggert, Bjoern Bourdon, Stefan Nolte, Joerg Rischmueller, and Mirco Imlau*

School of Physics, Osnabrück University, Barbarastr. 7, 49076 Osnabrück, Germany
*Corresponding author: mimlau@uos.de

Received 22 January 2018; revised 12 March 2018; accepted 13 March 2018; posted 14 March 2018 (Doc. ID 320238); published 2 May 2018

The role of chirp on the light–matter interaction of femto- and pico-second laser pulses with functional structured surfaces is studied using drag-reducing riblets as an example. The three-dimensional, periodic microstructure naturally gives rise to a mutual interplay of (i) reflection, (ii) scattering, and (iii) diffraction phenomena of incident coherent light. Furthermore, for femtosecond pulses, the structure induces (iv) an optical delay equivalent to a consecutive temporal delay of 230 fs in places of the pulse. These features enable studying experimentally and numerically the effect of tuning both pulse duration τ and spectral bandwidth $\Delta\omega$ on the features of the wide-angle scattering pattern from the riblet structure. As a result, we discovered a significant breakdown of fringes in the scattering pattern with decreasing pulse duration and/or increasing spectral bandwidth. This unique type of chirp control is straightforwardly explained and verified by numerical modeling considering the spectral and temporal interaction between different segments within the scattered, linearly chirped pulse and the particular geometric features of the riblet structure. The visibility of the fringe pattern can be precisely adjusted, and the off-state is achieved using $\tau < 230$ fs or $\Delta\omega > 2.85 \times 10^{13}$ rad/s.

OCIS codes: (120.4630) Optical inspection; (120.6650) Surface measurements, figure; (240.3695) Linear and nonlinear light scattering from surfaces; (280.4788) Optical sensing and sensors; (320.1590) Chirping; (320.2250) Femtosecond phenomena.
https://doi.org/10.1364/PRJ.6.000542

1. INTRODUCTION

Non-contact, laser-based optical sensors are crucial for the quality inspection of micro- and nano-structured surfaces in a variety of technological branches including the semiconductor industry (e.g., integrated circuit control), photonics industry (e.g., optics control), medical technology (e.g., hip joints), and automotive and aerospace fields (e.g., anti-fog and anti-icing surfaces) [1–5]. The approach to use femtosecond (fs) laser pulses as the probing light source in optical sensor technology is driven by the increasing economical availability of stable and high-power ultrashort pulse laser systems. At the same time, sub-picosecond-laser pulses represent a state-of-the-art working tool within a variety of production processes and enable fast and precise marking, cutting, soldering, and welding [6]. We here pursue the question of whether and how the use of ultrashort laser pulses in optical sensor technology may affect the measurement signal with the goal to improve the key measures that are used for quality inspection. A particular focus is given to the impact of the geometry of a relief structure on the wide-angle scattering of an incident, linearly chirped fs-laser pulse. We will therefore neglect the possible effect of a nonlinear optical response of the surface itself, as it may be expected due to high pulse peak intensities.

The drag-reducing riblet surface [cf. scanning electron microscope (SEM) image in Fig. 1(a)] serves as an example for our study. The interaction of continuous-wave, coherent light with riblet surfaces [cf. Fig. 1(a)] has been intensively studied for the purpose of quality inspection before [7–10]. Riblets obey their relevance in the engineering of drag reduction as they affect skin friction considerably [11–15]. The riblet functionality depends essentially on the integrity of the geometrical shape and therefore on the possibility to detect geometric alterations during production and maintenance with high precision in the submicrometer range at high sensing speed. The optical sensor described in Ref. [8] ensures these demands at high reliability due to a simple optical design [Fig. 1(b)]: a laser beam is incident normal to the riblet sample's surface, such that a wide-angle scattering pattern appears. The pattern consists of three main features in the $\pm 45°$ and $0°$ directions with respect to the sample's surface and in plane with the incoming beam in accordance with the triangular riblet structure and planes in between. Degradation of the riblets is measured as a decrease in the

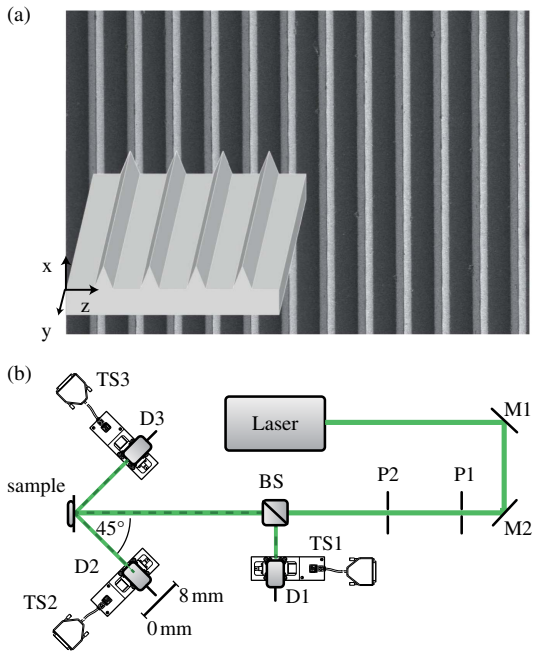

Fig. 1. (a) Scanning electron microscope (SEM) image and schematic, three-dimensional representation of the riblet structure under study. (b) Scheme of the optical setup of the riblet sensor described in Refs. [8,9]: the laser beam is incident normal to the riblet sample's surface, and the intensity distribution of the scattered light is detected in the 0° and ±45° directions. Degradation of the riblet structure is measured as a decrease in intensity around 45°. D1–D3, Si-PIN-diodes; BS, beam-splitter; M1, M2, mirrors; TS1–TS3, motorized translation stages.

intensity in the directions around 45°. Another characteristic of the scattered signal is the interference substructure [8] as a result from light diffraction at the periodic microstructure. It may be used for quality inspection as well [10] and contains information about riblet periodicity and duty cycle. However, we intend to disregard this signal due to signal fluctuations caused by the Moiré effect if fringe and detector array periodicities coincide [16].

One way to suppress the interference structure is to choose a detector diaphragm much larger than the fringe spacing. This strategy can be either realized by an appropriate Iris and/or distance between sample and photodiode. As a disadvantage, however, the dimensions of the optical setup are considerably extended, and the information about the riblet periodicity is lost.

In this work we introduce another strategy for the elimination of interference effects that is based on linearly chirped ultrashort laser pulses as the probing light source. The underlying idea is schematically sketched in Figs. 2(a) and 2(b): from ray-tracing considerations of an incident laser pulse onto a riblet structure, a difference of the optical path length in the ±45°-direction for waves reflected at neighboring flanks becomes obvious. This spatial delay can be estimated to about 70 μm for the given riblet structure under study ($\Lambda = 100$ μm, $h = 50$ μm). It corresponds with a temporal delay of about $\Delta t = 230$ fs. The latter is of importance if ultrashort laser pulses are used, in particular, if the pulse duration is in the order

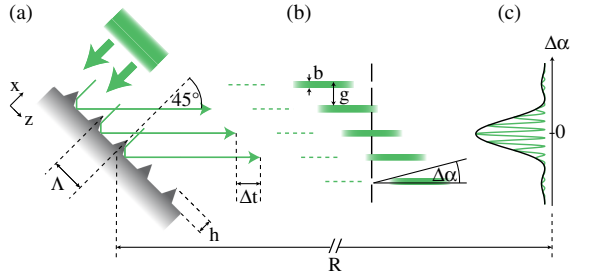

Fig. 2. (a) Scheme of the pulse front reflected in the 45° direction and distinct pulse path lengths from next-neighboring riblet flanks. Period Λ of the riblet structure is 100 μm, and riblet height h is 50 μm. The spatial delay induced by the riblet structure is 70 μm, and the correlated temporal delay is about $\Delta t = 230$ fs. (b) and (c) are discussed in the simulation section.

of magnitude of the temporal delay: when the pulse duration is adjusted below the temporal delay, $\tau < \Delta t$, the pulses do not overlap, and the interference should vanish.

In what follows, and based on these preconsiderations, we will examine differences between the following three probing approaches:

- probing with pulse durations $\tau < \Delta t$;
- probing with pulse durations $\tau > \Delta t$ and a broad frequency spectrum;
- probing with pulse durations $\tau > \Delta t$ and both decreasing pulse duration and frequency spectrum.

Both experimental and simulation methods are applied. Our comprehensive study shows that a complete disappearance of the interference at ±45° can be obtained. At the same time, it is possible to keep the interference in the scattering pattern in the direction around 0°. Thus, full access to analyze all important features of the riblet structure (periodicity, deviations of periodicity) is maintained. Furthermore, in analyzing the effect of pulse duration and bandwidth in more detail, we are able to precisely deduce the pulse characteristics for an all-optical control of the appearing wide-angle, scattering pattern. Thus, it becomes possible to choose between on and off states of the interference pattern by proper adjustment of the pulse parameters. Our results enable the redesign of the optical setup with much smaller dimensions while maintaining its reliability and precision. All our findings can be transferred to fs-pulse sensing of surface relief structures with different geometric shapes and dimensions, if the optical delay induced by the structure falls in the time region of the applied pulse duration.

2. EXPERIMENTS

A. Femtosecond Pulses and Simplified Pulse Shaping

We will use the following textbook knowledge about femtosecond pulses as fundament for our study: the time-bandwidth product $\Delta\omega \cdot \tau \geq 4 \ln 2$ for Gaussian-shaped pulses defines a minimum duration τ_0 for a given bandwidth based on the uncertainty principle. As an example, fs pulses in the visible spectral range with durations of $\tau = 50$ fs cover a bandwidth of more than 10 nm. A pulse that is close to the time-bandwidth product is called Fourier-limited, but it does not

preserve its shape when propagating through glass or several meters in air. Dispersion of the refractive index leads to different velocities of the spectral groups within the pulse, causing an extension of the pulse duration (group velocity dispersion) [17]. In the simplest case, a linear chirp results: $\omega(t) = \omega_0 + at$, with central frequency ω_0 and chirp parameter a. For what follows, it is important to note that the chirp parameter a, obtained via frequency gradient $a = \partial\omega/\partial t$, decreases as a function of increasing pulse duration of an incident pulse under the condition of a fixed bandwidth.

If the time-dependent frequency $\omega(t)$ is known, the spectral pulse shape can be transferred to a temporal pulse shape via Fourier transform and vice versa. In the following approach, the simplification

$$\frac{\partial\omega}{\partial t} = \frac{\Delta\omega}{\tau}\sqrt{1 - \left(\frac{\tau_0}{\tau}\right)^2} \approx \frac{\Delta\omega}{\tau} \tag{1}$$

is used to extract the frequency gradient from bandwidth and duration of a strongly chirped pulse $\tau_0/\tau \ll 1$.

Let us transfer this knowledge to design an optical setup for a proper experimental control. On the one hand, the magnitude of pulse chirp from dispersion can be varied by the thickness of the medium. On the other hand, the angular dispersion from prism and grating pairs is used so that the chirp is determined by the distance between them. This procedure is used in every pulse compressor/stretcher to achieve the desired pulse duration [18].

According to Eq. (1), for a fixed bandwidth, the pulse duration depends on the frequency gradient. But for strongly chirped pulses it is also possible to keep the frequency gradient fixed, so that the pulse duration depends on the bandwidth. Both processes are utilized in the following investigations to adapt the abovementioned dependencies.

The first applied method uses group velocity dispersion of borosilicate crown glass to extend the temporal profile by altering the pulse chirp while keeping the spectrum unchanged [cf. Eq. (1)]. A sketch of the experimental realization is shown in Fig. 3(a).

The second technique for fs-pulse shaping manipulates the spectral and temporal features of the pulse concurrently at constant pulse chirp inside a grating stretcher as shown in Fig. 3(b). The first grating BG1 decomposes the spectrum, and the second grating BG2 recollimates the beam while maintaining the spatial wavelength sort. A variable slit in the spatially dispersed spectrum cuts off the high- and low-frequency components [19,20]. Under the condition that the laser pulse is not bandwidth-limited, both the spectral bandwidth and the pulse duration are reduced as the slit width decreases. The advantage of this simplified setup is that an additional pulse duration stretch due to lenses and difficulties of chromatic aberration are eliminated [21].

B. Experimental Setups

An optical parametric amplifier (OPerA solo, Coherent Inc., USA) pumped by a regeneratively amplified Ti^{3+}:sapphire laser (Libra-F HE, Coherent Inc., USA) serves as the source for ultrashort laser pulses. The central wavelength is adjusted to $\lambda = 515$ nm, and the spectral bandwidth is

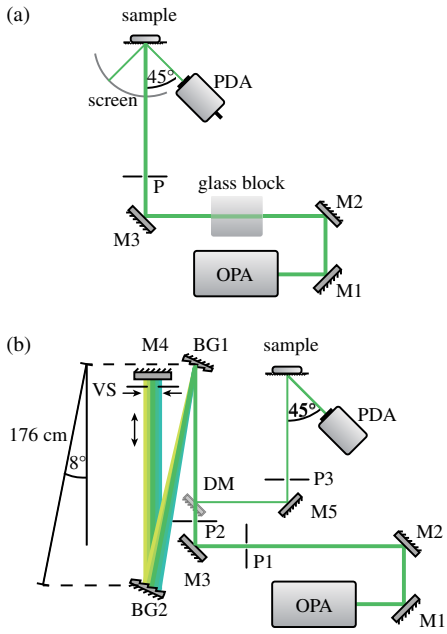

Fig. 3. (a) First setup: the laser beam is incident via mirrors M1–M3 normal to the riblet sample's surface and the scattered intensity pattern is observed on a screen or detected via a photodiode array in the 45° direction. The initial pulse duration is $\tau = 109$ fs. In order to expand the pulse duration, blocks of borosilicate crown glass are placed into the beam path. (b) Second setup: the laser beam is adjusted into a grating stretcher built of BG1, BG2, and M4. Distance between the two blazed gratings of 176(1) cm results in $\tau_2 = 2.4$ ps. The variable slit VS allows for a limitation of the effective bandwidth $\Delta\omega$ of the laser pulse. Its aperture a is varied from 1 to 7 mm. The D-shaped mirror DM separates incoming and stretched pulses. P1–P3 are pinholes to eliminate scattering.

$\Delta\omega = 3.56 \times 10^{13}$ rad/s, estimated via a fiber spectrometer (USB4000, Ocean Optics Inc., USA). In the first experimental setup, shown in Fig. 3(a), the laser beam is incident via mirrors M1–M3 normal to the riblet sample's surface, and the scattered intensity pattern is observed on a screen or detected via a photodiode array (S3902-512Q, Hamamatsu Photonics K.K., Japan) in the 45° direction at a distance between sample and detector of 36.0(5) cm. A pinhole limits the incident beam diameter to $d = (1.0 \pm 0.1)$ mm. The initial pulse duration is estimated via an autocorrelator (pulseCheck 15, APE, Germany) to be $\tau = 109(5)$ fs.

In order to expand the pulse duration, blocks of borosilicate crown glass with edge lengths of 56, 131, 171, and 211 mm are placed into the beam path, resulting in pulse durations of 234(5), 370(5), 680(5), and 900(5) fs, respectively.

In Fig. 3(b), a scheme of the second experimental setup is shown. The same laser beam as used above is adjusted into a double grating setup built of BG1, BG2, and M4 that stretches the pulse duration as a function of the distance between the two blazed diffraction gratings BG1 and BG2, blaze wavelength $\lambda_b = 500$ nm, and line spacing $1/d = 300$ mm^{-1} (GR25-0305, Thorlabs, Inc., USA) [18]. The distance between the two blazed gratings is adjusted to 176(1) cm, resulting in a measured stretch of pulse duration of $\tau = 2.4(1)$ ps. In our

Table 1. Slit Apertures a, Pulse Duration τ, and Spectral Bandwidth $\Delta\omega$[a]

Slit Aperture a (mm)	Pulse Duration τ (ps)	Spectral Bandwidth $\Delta\omega$ (rad/s)	$\Omega\tau$
7.0(1)	2.40(10)	3.56×10^{13}	8.18
6.0(1)	2.30(10)	3.56×10^{13}	8.18
5.0(1)	2.25(10)	2.85×10^{13}	6.55
4.0(1)	2.00(10)	2.35×10^{13}	5.40
3.0(1)	1.70(10)	2.42×10^{13}	5.56
2.0(1)	1.25(20)	2.06×10^{13}	4.75
1.0(1)	0.90(20)	1.92×10^{13}	4.42

[a]The product $\Omega\tau$ is depicted in the discussion.

experiment, the product $\Delta\omega \cdot \tau \geq 17$ and is therefore well above the bandwidth limit. The variable slit VS allows for a limitation of the effective bandwidth $\Delta\omega$ of the laser pulse. Its aperture a is varied from 1 to 7 mm. The D-shaped mirror DM separates the incoming and stretched pulses. The hereby resulting pulse durations and spectral bandwidths are measured via autocorrelator and spectrometer, respectively; an overview is presented in Table 1. The D-shaped mirror DM separates the incoming and stretched pulses. The scattered intensity is measured around 45° by a photodiode array device (S3902-512Q, Hamamatsu Photonics K.K.) with a spatial resolution of approximately 202 pixels/cm, and the distance between sample and detector is 36.0(5) cm. The spectral bandwidth decreases with the slit aperture. It is understandable that the pulse duration, which is initially determined by the stretching induced by the two gratings, is decreased when the maximal and minimal wavelengths are cut off, provided the pulse is not Fourier-transform-limited.

3. RESULTS

A. Experimental Results

Figure 4(a) shows the intensity pattern of the 45° signal obtained with the first setup for pulse durations of (1) 109 fs, (2) 234 fs, (3) 370 fs, (4) 680 fs, and (5) 900 fs, respectively. At all pulse lengths, the intensity distribution is consistent and shows no substructure. The visual appearance of this intensity pattern is shown in the screen photograph in Fig. 4(b) at $\tau = 900$ fs and accordingly shows a smooth appearance. This finding is in contrast to the observable substructure of the 45° signal in Fig. 4(d), obtained with a continuous-wave laser (Compass 215M-75, $\lambda = 532$ nm, Coherent Inc., USA) and well-known from previous experiments [7–9]. In the 0° direction, both intensity patterns in Figs. 4(c) and 4(e) show distinct interference features with three prominent center peaks.

In the setup of Fig. 3(b), the fringe pattern is studied as a function of slit aperture a as depicted in Fig. 5. For a slit aperture of $a = 7$ mm, a smooth intensity distribution is visible as found in Figs. 4(a) and 4(b). As the slit aperture decreases, the interference fades in towards a well-defined substructure at $a = 1$ mm.

The results of the detected intensity patterns for $a = 1$ mm and $a = 7$ mm are shown and fitted to the sum of two Gaussian functions. As suggested in Ref. [8], the area integral

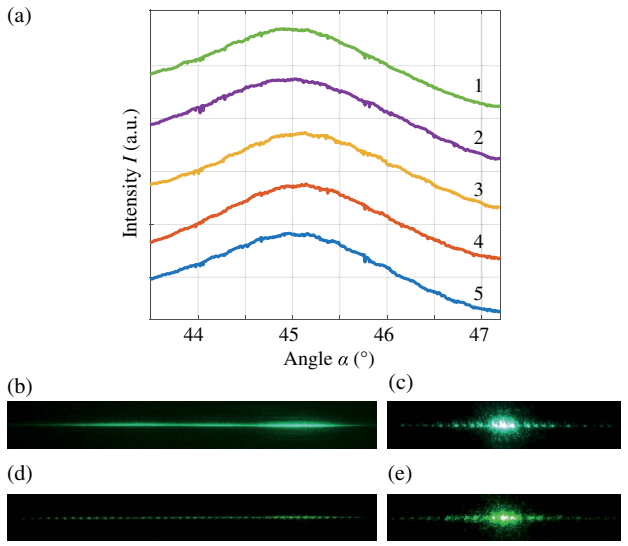

Fig. 4. (a) Intensity patterns of the 45° signal obtained with the first setup for pulse durations of (1) 109 fs, (2) 234 fs, (3) 370 fs, (4) 680 fs, and (5) 900 fs, respectively. (b)–(e) Photographs of the intensity patterns (b), (c) at 900 fs and (d), (e) with a continuous-wave laser ($\lambda = 532$ nm). (b) The 45° signal appears smoothly. This finding is in contrast to the observable substructure of the 45° signal well-known from continuous wave-experiments shown in (d). (c), (e) In 0° direction, both intensity patterns show distinct interference features with three prominent center peaks.

of the Gaussian graph is used for degradation. The data set furthermore reveals that the position of the fringe maxima is slightly displaced as a function of slit aperture. This effect can be attributed unambiguously to the spatial displacement of the laser beam induced by the mechanical changes in the slit aperture. As a result, the laser spot position is slightly displaced on the riblet sample, that in turn displaces the position of the fringe maxima on our detector array.

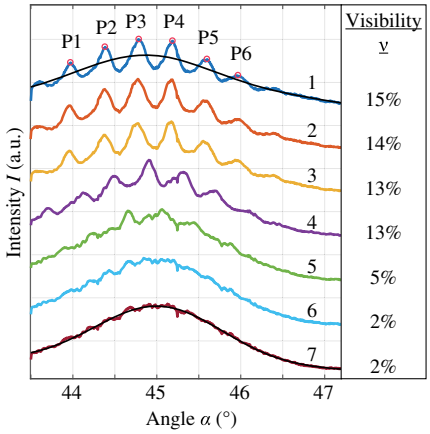

Fig. 5. Intensity pattern as a function of slit aperture a and accordingly labeled from 1 to 7. Smooth intensity distribution for $a = 7$ mm as found in Fig. 4(a). With decreasing slit aperture and consequently decreasing pulse duration and bandwidth, the interference pattern appears. The results of the detected intensity patterns for $a = 1$ mm and $a = 7$ mm are fitted to the sum of two Gaussian functions. On the right, the respective visibilities ν are specified.

Since the focus of this work is not on the evaluation of the degradation, but on the analysis of the interaction between chirped ultrashort pulses and the riblet structure, the fit parameters will not be discussed further. Rather, we turn to the appearance of interference. Related to the fringe pattern, we can define the interference by the contrast, namely given by the visibility ν

$$\nu = \frac{I_{\max} - I_{\min}}{I_{\max} + I_{\min}}. \tag{2}$$

It is determined by averaging the specific visibilities of the six main peaks of the pattern as marked in Fig. 5. The results for ν are listed in Fig. 5 and cover resulting visibility values between 2% and 15%.

B. Simulation

In what follows, we attempt to analyze in more detail the correlation of pulse duration, bandwidth, and fringe pattern in the 45° direction. For this purpose, we refer to Fig. 2(b) and introduce the periodicity g of light emission parallel to 45°, which is determined by the riblet period Λ: $g = \Lambda \cdot \sin 45°$, and width b of a single reflection, which is equal to the width of one riblet flank.

Under these conditions, the generated scattering pattern at distance R can be interpreted as a diffraction signal from a multiple slit as geometrically sketched in Figs. 2(a) and 2(b).

In order to simulate this intensity pattern we describe the time- and angle-dependent electrical field by a sum of a series of normalized plane waves as follows:

$$E(\Delta\alpha, t) = \sum_{n=1}^{N}\sum_{m=1}^{M} A_n(t_n)\exp[i(k_n R - (\omega_0 + \frac{1}{2}\dot{\omega}t_n)t_n + \phi_n + \phi_m)], \tag{3}$$

with

$$A_n(t_n) = \exp\left\{-\frac{2\left\{\left[n - \frac{1}{2}(N+1)\right]\Lambda\right\}^2}{w_r^2}\right\} \cdot \exp\left[-2(\ln 2)\frac{t_n^2}{\tau^2}\right], \tag{4}$$

$$t_n(t) = t - (n-1)\cdot\Delta t, \tag{5}$$

$$\omega_n(t_n) = \omega_0 + \dot{\omega}\cdot t_n, \tag{6}$$

$$\phi_n(\omega_n) = \frac{\omega_n}{c}\cdot\sin(45° + \Delta\alpha)\Lambda\cdot\sin 45°\cdot(n-1), \tag{7}$$

$$\phi_m(\omega_n) = \frac{\omega_n}{c}\cdot\sin(45° + \Delta\alpha)\frac{b}{M-1}\cdot(m-1). \tag{8}$$

The natural numbers N and M thereby describe the number of slits and the number of reflected waves at each slit, respectively. The term A_n determines the Gaussian-shaped envelope amplitude based on the transversal beam waist w_r [at exp(−2) intensity] and the pulse duration τ (full width at half-maximum, FWHM). The time t_n is a function of the slit number n because of the consecutive delay Δt. The frequency ω_n is a function of time, respecting the frequency gradient $\partial\omega/\partial t$, that results in a time dependence of the wave vector $k_n = \omega_n/c$ as well (c is the speed of light). The phase differences $\phi_{n,m}$ are determined by wave vectors k_n as a function of time due to pulse chirp, besides the geometrical conditions, namely Λ, b, R, and angle of observation $\Delta\alpha$.

Integration of Eq. (3) over time then yields the energy density pattern $W(\Delta\alpha)$

$$W(\Delta\alpha) = \int |E(\Delta\alpha, t)|^2 \mathrm{d}t. \tag{9}$$

With this model, it is possible to simulate both of the experimental setups. We like to note that based on Eq. (1), the frequency gradient, bandwidth, and pulse duration are coupled in a way that it is not possible to separately change one of them. Therefore the pulse duration τ can only be altered in expense of the frequency gradient $\partial\omega/\partial t$ [Fig. 6(a)] or the bandwidth $\Delta\omega$ [Fig. 6(b)].

Figure 6 shows the results of the simulations based on Eq. (9) for the bandwidth and frequency gradient according to the experiment. No interference effects are visible when changing the pulse duration, and thus the frequency gradient, at a constant bandwidth [Fig. 6(a)]. However, changing the bandwidth, and thus the pulse duration, at a constant frequency gradient reveals a different picture [Fig. 6(b)]: a diffraction pattern appears in a certain window of bandwidths between $\Delta\omega \approx (0.3\text{–}2.2) \times 10^{13}$ rad/s and pulse durations between $\tau \approx 200\text{–}1500$ fs.

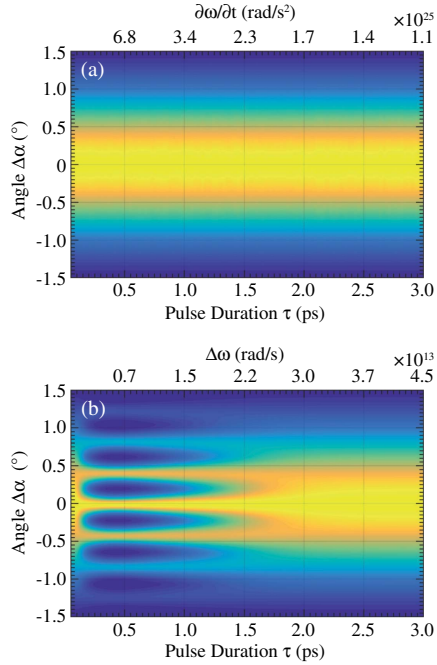

Fig. 6. Numeric energy pattern $W(\Delta\alpha)$ for 45° (a) for a constant bandwidth of $\Delta\omega = 3.41 \times 10^{13}$ rad/s ($\Delta\lambda = 4.8$ nm) and variable pulse duration τ and frequency gradient $\partial\omega/\partial t$, and (b) for a constant frequency gradient $\partial\omega/\partial t = 1.49 \times 10^{25}$ rad/s^2 and variable pulse duration τ and bandwidth $\Delta\omega$ ($N = 13$, $M = 5$, $b = 15$ µm, $\Lambda = 100$ µm, $R = 0.36$ m).

The calculations were also applied to the direct reflection signal in the 0° direction. In this case, a stationary interference pattern is formed regardless of the chosen parameters for pulse duration τ and bandwidth $\Delta\omega$ (not shown).

4. DISCUSSION

The results of the experiments and the simulation are consistent with each other, and the observed phenomena can be explained on the basis of temporal pulse sequences and interference.

In the 0° direction, the interference pattern is distinctly visible and can be directly attributed to the model of a multiple slit only. This signal originates from perpendicular reflection at the riblet plains, so that no optical path difference is induced in this direction ($\Delta t = 0$, cf. Ref. [9]). In the case of a linearly chirped pulse, the same frequencies simultaneously reach the detector while the chirp is maintained. This case is comparable to probing with continuous-wave light of bandwidth $\Delta\omega$.

In the 45° direction, we can distinguish between three cases. In the simplest case, the pulse duration τ is below the temporal delay Δt, and therefore there is no overlap of next-neighbouring pulse sections, i.e., no interference. The other two cases are depicted in Figs. 7(a) and 7(b) and represent the first [cf. Fig. 3(a)] and second experimental setup [cf. Fig. 3(b)] at $\tau = 900$ fs, respectively.

Shown is a plot of frequency ω and power P versus time for two next-neighbouring pulses with a mutual temporal delay of 230 fs. The slope of frequency is $\partial\omega/\partial t = \Delta\omega/\tau$.

The pulse durations in Figs. 7(a) and 7(b) are similar, whereas the bandwidths are different: $\Delta\omega_a > \Delta\omega_b$, and thus the frequency gradient $\partial\omega/\partial t$ in Fig. 7(a) is larger. Therefore, the difference Ω_a of superposing frequencies is high, and no stationary interference pattern is formed [21]. With decreasing

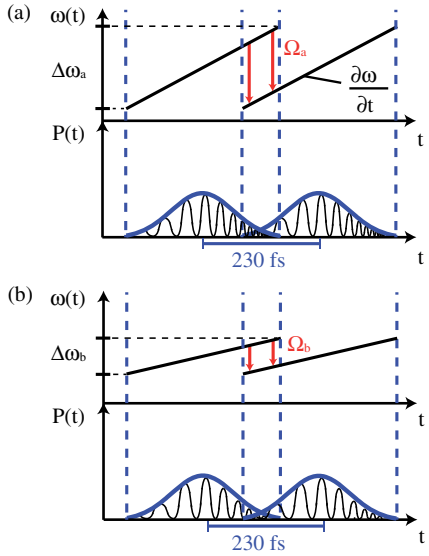

Fig. 7. Plot of frequency ω and power P versus time for two next-neighboring pulses with a mutual temporal delay of 230 fs. Slope of frequency is $\partial\omega/\partial t = \Delta\omega/\tau$. (a) Frequency detuning Ω_a for overlapping pulses. (b) Same pulse duration as in (a), while bandwidth is decreased, which results in the appearance of a stationary interference pattern.

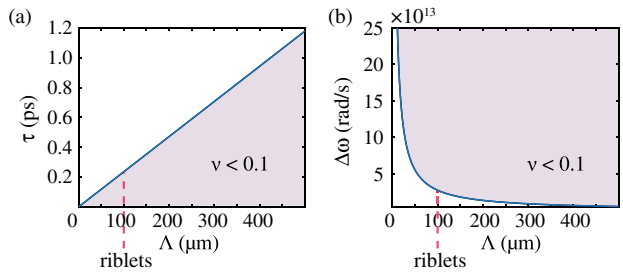

Fig. 8. Influence of structure period Λ on threshold values of (a) pulse duration τ and (b) bandwidth $\Delta\omega$ for a vanishing interference pattern ($\nu < 0.1$). Characteristic period $\Lambda = 100$ μm of the investigated riblet structure is marked, respectively.

bandwidth of the pulse $\Delta\omega_b < \Delta\omega_a$ [cf. Fig. 7(b)], the interference pattern appears (cf. Fig. 5) as the frequency difference Ω_b is reduced: $\Omega_b < \Omega_a$. The latter is determined by pulse duration τ and bandwidth $\Delta\omega$ or frequency gradient of the pulses $\partial\omega/\partial t$

$$\Omega = \frac{\Delta\omega}{\tau} \cdot \Delta t = \frac{\partial\omega}{\partial t} \cdot \Delta t. \tag{10}$$

For interference, however, Ω alone is not decisive but rather the product $\Omega\tau$. This is illustrated by the second experiment where the frequency gradient $\partial\omega/\partial t$ is constant and thus also $\Omega(t)$, but the visibility of the interference pattern differs essentially. As a condition for interference, an upper boundary value for the product $\Omega\tau$ can be estimated [22]. The values for $\Omega\tau$ of our experiments are depicted in Table 1. Concluding these considerations, the appearance of the interference can be adjusted via the pulse parameters. We note that further parameters may be deduced from the dependence of the scattering features on pulse duration and bandwidth, e.g., the determination of the pulse chirp from the fringe visibility. For this purpose and a sufficient precision, however, it will be necessary to make a point of improving the fringe contrast by appropriate laser (intensity, coherence length, etc.) and/or riblet (periodicity, riblet height, etc.) parameters.

For the particular case of a fixed temporal delay Δt, the product $\Omega\tau$ reads

$$\Omega\tau \le C \Leftrightarrow \Delta\omega \le \frac{C}{\Delta t}. \tag{11}$$

Constant C can be drawn from the measurement data. For a vanishing interference contrast of less than 10%, $\Delta\omega > 2.85 \times 10^{13}$ rad/s is valid, which corresponds to $C = 6.56$.

In Fig. 8 the influence of structure period Λ on the threshold values of pulse duration τ and bandwidth $\Delta\omega$ for a vanishing interference pattern ($\nu < 0.1$) is depicted for $C = 6.56$.

The investigations show clearly that the impact on measurements signals needs to be considered when using a chirped ultrashort laser pulse. In general, one can expect an influence on interference when a temporal delay Δt is induced to fractions of the chirped pulses by a microstructure. Besides the simple case with $\tau < \Delta t$, the choice of bandwidth and chirp affect the appearance of interference effects as well. According to the goal of

our study, we were able to suppress the fringe pattern that overlays with the scattering pattern.

5. CONCLUSIONS

We have introduced the chirp as a novel parameter for the all-optical control of a wide-angle scattering pattern with a drag-reducing riblet structure as an example. In our particular example, we are able to deduce precise requirements for a smooth measurement signal in the 45° direction with a visibility of the interference $\nu < 0.1$ (pulse duration $\tau < 230$ fs or bandwidth $\Delta\omega > 2.85 \times 10^{13}$ rad/s for linearly chirped pulses). The vanishing of the interference substructure as main objective of our study enables the use of a photodiode array within the riblet sensor. This results in an effective improvement of the measurement speed and the possibility to redesign the optical sensor setup with much smaller dimensions. Reliability and precision of the sensor are maintained. It is noteworthy that a standard fs-pulse laser implemented into the riblet sensor fulfills the requirements for a smooth intensity signal in the 45° direction. All our considerations can be easily transferred to similar structured surfaces and specific limit values can be obtained if the optical delay induced by the geometric structure coincides with the pulse duration.

Funding. Seventh Framework Programme (FP7) (CSJU-GAM-SFWA-2008- 001); Deutsche Forschungsgemeinschaft (DFG); European Union's Seventh Framework Program (FP7/2007-2013); Clean Sky Joint Technology Initiative (CSJU-GAM-SFWA-2008-001).

Acknowledgment. The authors acknowledge financial support by the European Union's Seventh Framework Program for the Clean Sky Joint Technology Initiative. We acknowledge support by Deutsche Forschungsgemeinschaft (DFG) and Open Access Publishing Fund of Osnabrück University.

REFERENCES

1. M. M. Moslehi, "Sensor for semiconductor device manufacturing process control," U.S. patent 5,293,216 (March 8, 1994).
2. M. M. Moslehi, "Apparatus for semiconductor device fabrication diagnosis and prognosis," U.S. patent 5,719,495 (February 17, 1998).
3. J.-H. Lee, J. P. Singer, and E. L. Thomas, "Micro-/nanostructured mechanical metamaterials," Adv. Mater. **24**, 4782–4810 (2012).
4. B. Kasemo, "Biological surface science," Surf. Sci. **500**, 656–677 (2002).
5. V. A. Ganesh, H. K. Raut, A. S. Nair, and S. Ramakrishna, "A review on self-cleaning coatings," J. Mater. Chem. **21**, 16304–16322 (2011).
6. J. Ion, *Laser Processing of Engineering Materials: Principles, Procedure and Industrial Application* (Butterworth-Heinemann, 2005).
7. M. Imlau, H. Brüning, K.-M. Voit, J. Tschentscher, S. Dieckhoff, U. Meyer, K. Brune, J. Derksen, and C. Tornow, "A method for quality control of a micro-structuring and apparatus therefor," DE102013220006A1 (April 2, 2015).
8. M. Imlau, H. Bruening, K.-M. Voit, J. Tschentscher, and V. Dieckmann, "Riblet sensor—light scattering on micro structured surface coatings," arXiv: 1601.04694 (2016).
9. J. Tschentscher, S. Hochheim, H. Bruening, K. Brune, K.-M. Voit, and M. Imlau, "Optical riblet sensor: beam parameter requirements for the probing laser source," Sensors **16**, 458 (2016).
10. U. Meyer, S. Markus, and S. Dieckhoff, "Device for testing the quality of microstructurization," U.S. patent 8,842,271 (September 23, 2014).
11. D. W. Bechert, M. Bruse, W. Hage, J. G. T. van der Hoeven, and G. Hoppe, "Experiments on drag-reducing surfaces and their optimization with an adjustable geometry," J. Fluid Mech. **338**, 59–87 (1997).
12. M. Bruse, D. Bechert, J. T. van der Hoeven, W. Hage, and G. Hoppe, "Experiments with conventional and with novel adjustable drag-reducing surfaces," in *Proceedings of the International Conference on Near-Wall Turbulent Flows*, Tempe, Arizona (March 15–17, 1993), pp. 719–738.
13. M. J. Walsh, "Effect of detailed surface geometry on riblet drag reduction performance," J. Aircr. **27**, 572–573 (1990).
14. D. W. Bechert, M. Bruse, W. Hage, and R. Meyer, "Fluid mechanics of biological surfaces and their technological application," Naturwissenschaften **87**, 157–171 (2000).
15. B. Dean and B. Bhushan, "Shark-skin surfaces for fluid-drag reduction in turbulent flow: a review," Philos. Trans. R. Soc. London A **368**, 4775–4806 (2010).
16. G. C. Holst, *CCD Arrays, Cameras, and Displays* (JCD, 1998).
17. L. Brillouin, *Wave Propagation and Group Velocity* (Academic, 2013), Vol. **8**.
18. E. Treacy, "Optical pulse compression with diffraction gratings," IEEE J. Quantum Electron. **5**, 454–458 (1969).
19. J. P. Heritage, R. N. Thurston, W. J. Tomlinson, A. M. Weiner, and R. H. Stolen, "Spectral windowing of frequency-modulated optical pulses in a grating compressor," Appl. Phys. Lett. **47**, 87–89 (1985).
20. J. P. Heritage, A. M. Weiner, and R. N. Thurston, "Picosecond pulse shaping by spectral phase and amplitude manipulation," Opt. Lett. **10**, 609–611 (1985).
21. A. M. Weiner, "Ultrafast optical pulse shaping: a tutorial review," Opt. Commun. **284**, 3669–3692 (2011).
22. S. Odoulov, A. Shumelyuk, H. Badorreck, S. Nolte, K.-M. Voit, and M. Imlau, "Interference and holography with femtosecond laser pulses of different colours," Nat. Commun. **6**, 5866 (2015).